Thermal decomposition and recovery properties of ZnAl–CO 3 layered double hydroxide for anionic dye adsorption: insight into the aggregative nucleation and growth mechanism of the LDH memory effect.

R. M M Santos, J. Tronto, V. Briois, C. V Santilli

Journal of Materials Chemistry A

ARTICLE

Thermal decomposition and recovery properties of ZnAl-CO_3 layered double hydroxide for anionic dye adsorption: Insight of the aggregative nucleation and growth mechanism of LDH memory effect.

Received 00th January 20xx,
Accepted 00th January 20xx

DOI: 10.1039/x0xx00000x

www.rsc.org/MaterialsA

R. M. M. Santos[a*], J. Tronto[b], V. Briois[c], C. V. Santilli[a*]

Abstract: The thermal decomposition of carbonate-intercalated layered double hydroxide (ZnAl-CO_3-LDH) and recovery induced by water and dye solution addition were studied *in situ* by time-resolved Wide Angle X-ray Scattering (WAXS) and time-resolved X-ray Absorption Spectroscopy (XAS), providing insights on the mechanisms of these structural transformations. LDH nanostructure recovery was driven by an aggregative nucleation and growth mechanism, which is limited by the steric hindrance, caused by the adsorption of the Acid Blue 113 azo dye (AB) in external surface of both the nanocrystalline tactoids and the exfoliated layers. The recovery behaviour in dye solution is consistent with the hypothesis of the LDH-recovery by a direct synthesis process, generating nanosized LDH particles with thickness about four times lower than those induced by water addition. These findings explain the higher AB adsorption capacity (1587 $mg{\cdot}g^{-1}$) of calcined LDH compared to pristine ZnAl-CO_3-LDH (261.8 $mg{\cdot}g^{-1}$) and also the efficient recycling of the spent adsorbent.

1. Introduction

The increasing demand for new products and technological developments influences our modern society and spurs many industries to use synthetic chemicals. In many cases, this gives rise to the creation of pollutants and the production of by-products which might become complex environmental problems. Synthetic dye pollution is produced by dye industries and results from their industrial uses in textiles, dyeing, paints and printing, in food and pharmaceutical or cosmetic applications, in metallurgy, plastics, agro-chemistry, and others.[1]

In aquatic environments, the toxicity of these compounds has been detrimental to various life forms, causing visual pollution in addition to seriously damaging flora and fauna.[2] Because of these environmental consequences, new processes of removing and degrading these compounds in effluents have been studied, taking into account the economic factors and chemical efficiency of each process. For this purpose, biological treatment,[3] adsorption,[4] degradation,[5] microfiltration[6] and ozonation[7] are usually used to remove organic compounds from industrial wastewater. The adsorption process has wide industrial applicability since it combines low cost and high removal rates. Moreover, in some cases, it allows the recovery of adsorbed species without the loss of their chemical identity.[8]

Layered Double Hydroxides (LDH) are described by the general formula: $[M^{2+}_{(1-x)}M^{3+}_{x}(OH)_2]_{layer}\ [A^{n-}_{x/n}{\cdot}zH_2O]_{interlayer}$, where M^{2+} and M^{3+} are divalent and trivalent metal cations occupying the octahedral interstices of layers, while A^{n-} represents organic or inorganic anions embedded in the interlayers of the lamellar edifice (Fig. 1). LDH are a family of anionic clays that have received attention over the past decades because of their important applications in several fields such as adsorption,[9] catalysis,[10] chemical additives,[11] drug delivery[12] and others. Their adsorption capacity is related to the presence of positively charged sites on the surfaces of layers, as well as appropriate porosity and specific surface area, which support the process. Furthermore, when calcined LDH are used as adsorbents, the extraction capacity of the anionic species may be exceeded by the additional possibility of internal sites occupation, known as sorption process.[13-15]

[a] Universidade Estadual Paulista (UNESP), Instituto de Química. Rua Prof. Francisco Degni, 55, 14800-060, Araraquara-SP, Brazil.
[b] Instituto de Ciências Exatas e Tecnológicas, Universidade Federal de Viçosa, Campus de Rio Paranaíba. Rodovia BR 354, km 310, 38810-000, Rio Paranaíba-MG, Brazil.
[c] Synchrotron SOLEIL, CNRS-UR1, L'Orme des Merisiers, BP48, Saint-Aubin, 91192, Gif-sur Yvette, France.

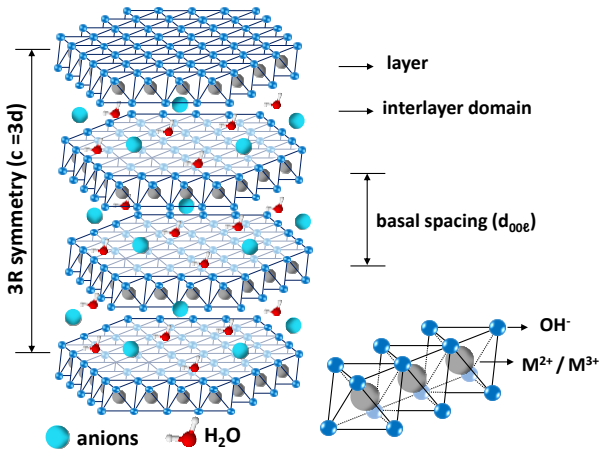

Fig. 1 Schematic structure of layered double hydroxides (LDH).

Upon thermal decomposition of LDH, mixed oxide-hydroxide phases involving di- and tri-valent metals are formed with good dispersion in the final material associated to the metal component inter-dispersion in the pristine LDH.[10] The increase in specific surface area and porosity resulting from this decomposition leads to technologically important materials, particularly in the fields of catalysis and adsorption processes. [10] Additionally, the metastable mixed oxides formed by the calcination at moderate temperatures (400-500°C), can recover the layered structure when put in contact with water or an anionic solution.[16] This behaviour is often referred to as the "*memory effect*", which provides some interesting advantages for pollutant removal.[15] This reversible transformation remains a topic of intense debate in the literature. Millange *et al.*[17] studied the *in situ* recovery of Mg-Al-LDH by time-resolved energy dispersive X-ray diffraction, and proposed that the recovery occurs in two stages: partial oxide dissolution, followed by LDH recrystallization from the solution. On the other hand, Sato *et al.*[18] suggested that the structural recovery occurs topotactically, without dissolution. Moreover, Mascolo and Mascolo[16] described the "*memory effect*" as a simple direct synthesis from the metastable oxide precursors, since they are often poorly crystalline, highly reactive and are homogeneously mixed at the atomic level.

There are several works in the literature showing a notable increase in adsorption capacity of anionic species by calcined LDH compared to the pristine carbonate-intercalated LDH.[13, 15, 19, 20] This feature is generally attributed to the larger specific surface area of the calcined material compared to the pristine LDH,[19, 20] and to the structural recovery property, allowing the dye intercalation process.[13, 14] Moreover, the lower anion uptake by pristine LDH is mainly attributed to exclusive adsorption onto the external surfaces of the particles, neglecting not only the effect of the different structure and texture between pristine LDH and recovered one,[16] but also the growth mechanisms involved on this transformation. In a few papers,[13, 14, 19-21] the correlation between these structural parameters, the recovery mechanisms and the dye uptake capacity are invoked without direct experimental evidences.

This paper compares the Acid Blue 113 (AB) dye adsorption kinetics of calcined and pristine ZnAl-CO_3-LDH and discusses in depth the correlation between the dye uptake and recovery mechanisms supported by kinetic laws derived from structural parameters determined from *in situ* and time-resolved synchrotron-based measurements. Those techniques unravelling the local and medium range order modifications of these materials upon calcination and the structural recovery induced by water and dye solution contact, were used to establish relationships between structural and adsorption properties of these materials. From these experimental results we demonstrated that the AB dye adsorption on the external surface of the LDH lamellae strongly limits the particle growth through aggregative mechanism, increasing the adsorption capacity of organic anionic species.

2. Experimental

2.1. LDH preparation

The ZnAl-CO_3-LDH was prepared using the coprecipitation method at room temperature (RT) as follows:[22] a 48.0 mmol of $Zn(NO_3)_2$ and 24.0 mmol of $Al(NO_3)_3$ aqueous solution (0.25 L) was added dropwise to a 48.0 mmol of Na_2CO_3 solution (1.25 L) under vigorous stirring. The mixture was maintained at pH 8 by adding 2 $mol{\cdot}L^{-1}$ NaOH aqueous solution during precipitation. The Zn:Al atomic ratio in the starting solution was adjusted to 2:1. The resulting precipitate was aged for 12 h under stirring. The precipitate was then isolated by filtration, washed thoroughly with deionized water several times and dried at reduced pressure in the presence of silica gel at room temperature (RT ≈ 25°C).

2.2. Mixed oxides preparation

In order to obtain mixed oxides of the metal components, the prepared LDH was calcined at 450 °C at 10 $°C{\cdot}min^{-1}$ heating rate and 100 $cm^3{\cdot}min^{-1}$ air flow for 30 min. These materials were characterised and used in adsorption experiments. This sample is nominated hereafter as Calc-LDH.

2.3. Characterisation of LDH and Calc-LDH

LDH and Calc-LDH samples were characterised by X-ray powder diffraction (XRPD) with a Shimadzu XRD-6000 diffractometer using Cu Kα radiation (λ = 1.5406 Å) monochromatized by a graphite single crystal.

The specific surface area and sample porosity were determined by nitrogen adsorption and desorption at the liquid nitrogen boiling temperature (-196 °C) and relative pressure interval between 0.001 and 0.998, with an isotherms analyser ASAP 2010 (Micromeritics). For this purpose, a sample outgassing was performed under vacuum (≈10 μPa) at 150 °C for 12 h. The Brunauer-Emmett-Teller (BET) equation was used to calculate the specific surface area and the pore-size distribution was derived from the desorption branch of the isotherm using the Barrett-Joyner-Halenda (BJH) method.[23]

Thermogravimetric curves were recorded on SDT Q600 TA Instruments (TG) at a temperature range from RT to 700 °C at a 10 °C·min^{-1} heating rate and 100 cm^3·min^{-1} air flow.

The microstructures of the samples were observed with a scanning electron microscope (SEM) (XL-30, Philips) and a transmission electron microscope (TEM) (100CXII, JEOL). For SEM analyses, samples were deposited on conductive double-sided carbon tape and sputtered with gold. For TEM analysis, a droplet of diluted nanoparticles suspended in 2-propanol was deposited on a carbon-coated copper grid. For particle size analysis it was employed the ImageJ software.[24]

2.4. Synchrotron-based characterisations

Wide Angle X-ray Scattering (WAXS) investigation of LDH thermal decomposition and recovery was carried out at the SAXS beam line of the Brazilian National Synchrotron Laboratory (LNLS) to examine the changes of long range structural order. For the thermal decomposition experiments, samples were placed in quartz capillaries and heated from RT to 450 °C on a LINKAM (THMS600) heating and cooling stage with a heating ramp of 10 °C·min^{-1}. For regeneration experiments, the Calc-LDH sample was placed in the sample holder at RT, then water or 1000 mg·L^{-1} AB dye solution was added to impregnate the powder. Measurements were taken for 1 h.

X-ray absorption spectroscopy (XAS) provides detailed information about the local order of a selected absorbing atom, in this case zinc, as well as its electronic structure. The use of the Quick-XAS technique allows for characterising the transformation of the absorbing atom during a physical-chemical process with a high time-resolution. Quick-XAS characterisation during the thermal decomposition and regeneration process of the LDH were collected at the ROCK beamline at the Synchrotron SOLEIL (France).[25] Quick-XAS spectra were acquired at the Zn K-edge (9659 eV) with a 2 Hz oscillation frequency of the Si(111) channel-cut, leading to recording at 0.5 s two XAS spectra per turn of the cam driving the tilt table, which supports the crystal (one spectrum with increasing energy and a second with decreasing energy).[26] The samples were placed in a home-made oven [27] and the temperature was increased to 450 °C (10 °C·min^{-1} heating ramp) to monitor the local order changes in LDH structure by Quick-XAS. Afterward, the calcined sample was cooled to RT and put in contact with water or 1000 mg·L^{-1} AB dye solution to follow the local order changes during the recovery process.

Energy calibration and normalization procedure of raw XAS data were first carried out using a Python GUI developed at the ROCK beamline dedicated to the handling of hundreds of spectra in a couple of seconds. The time-resolved normalized XAS dataset was analysed by Multivariate Curve Resolution with Alternating Least Squares (MCR-ALS) fitting analysis[28] and Principal Component Analysis (PCA) using the MCR-ALS GUI 2.0 free toolbox developed by Tauler *et al.* on the Matlab® platform.[28] The MCR-ALS method applied to XAS was detailed in recent papers[29-32] and briefly summarized as supporting information. EXAFS extraction and Fourier transformation of selected XAS data, together with the fitting of EXAFS spectra of LDH and Calc-LDH recorded at RT, were done using the Athena/Artemis software package.[33]

2.5 Dye adsorption studies on LDH and Calc-LDH

Suspensions were prepared by adding 10 mg of LDH or Calc-LDH to 20 mL of dye solutions with different concentrations (100 to 1600 mg·L^{-1}). The suspensions were placed in a thermostatic bath heated to different temperatures (25, 30, 35 and 40 °C), under 240 rpm stirring. Aliquots were collected at different time intervals (60 to 420 min).

For the adsorption studies, the anionic azo dye Acid Blue 113 (Luganil® Dark Blue NB) purchased from BASF industry (Porto Alegre-RS, Brazil) was used without further purification. The dye concentration in the supernatant solution was determined by UV-Vis absorption spectrophotometry at λ_{max} = 581 nm, using a Cary 60 UV-Vis spectrophotometer (Agilent).

The point analysed at 420 min for each temperature was taken as the equilibrium dye concentration C_e (mg·L^{-1}) since it does not present a significant difference compared to the preceding point. This point was used in the adsorption isotherms construction. The amount of dye adsorbed at the equilibrium (q_e, mg·g^{-1}), was calculated according to eqn. 1:

$$q_e = V \cdot \frac{(C_0 - C_e)}{m} \quad (1)$$

where C_0 is the initial dye concentration (mg·L^{-1}), V is the dye solution volume (L) and m is the LDH or Calc-LDH mass (g).

In order to examine the mechanisms that control the adsorption process, such as mass transfer in the solution and adsorbent/adsorbate interactions, several kinetic models were tested to interpret the experimental data. Pseudo-first order (eqn. 2) and pseudo-second order (eqn. 3) are among the most commonly applied models in the kinetic study of adsorption processes for solid/liquid interfaces.[34] Thus, the correlation coefficient and the linear fit of each kinetic equation applied to the experimental data were used to interpret the dye adsorption mechanism of the solid phase.

$$log(q_e - q_t) = log q_e - \frac{k_1}{2.303} t \quad (2)$$

$$\frac{t}{q_t} = \frac{1}{k_2 {q_e}^2} + \frac{1}{q_e} t \quad (3)$$

where q_t is the adsorbed mass per adsorbent unit mass at the time t (min); k_1 and k_2 are the rate constants of first and second-orders.

To calculate thermodynamic extensive properties related to the adsorption process, $\Delta H°$, $\Delta S°$ and $\Delta G°$, eqns. 4 and 5 were used:

$$\Delta G^\circ = -RT \cdot ln k_{ad} \quad (4)$$

$$ln k_{ad} = -\Delta H^\circ / RT + \Delta S^\circ / R \quad (5)$$

where k_{ad} is the Langmuir equilibrium constant, obtained by the adsorption isotherms (k_L, L·mg^{-1}) multiplied by the density of water (10^6 mg·L^{-1}) and R is the universal gas constant (8.31446 J·K^{-1}·mol^{-1}).[35]

The recyclability of the adsorbent was evaluated by repeated adsorption/calcination cycles using the same Calc-LDH sample. A constant Calc-LDH dosage of 500 mg·L^{-1} was placed in 100 mg·L^{-1} AB solutions at 25 °C and kept in contact for 420 min. The used Calc-LDH powder was calcined and reused in the same conditions. This procedure was repeated five times and the adsorption capacity was calculated for each cycle.

3. Results and discussion

3.1. LDH and Calc-LDH characteristics

Fig. 2 shows the X-ray diffractograms of the pristine LDH and Calc-LDH. In order to compare the positions of the peaks with those recorded by WAXS, a double scale is used for the abscissa with the 2θ Bragg angles at the bottom and the scattering q vector calculated from the relationship $q\lambda = 4\pi \cdot \sin\theta$ at the top. In Fig. 2a, it is possible to note the presence of basal peaks (00ℓ) [(003), (006) and (009)], which are related to the stacking planes of lamellae, characteristic of the LDH structure. The basal spacing distance ($d_{00\ell} = 2\pi / q$) calculated from the q position of the (003) and (006) peaks was 7.54 Å, coinciding with the value observed for carbonate intercalation in LDH.[36] After LDH calcination (Calc-LDH) the collapsed lamellar structure (Fig. 2b) was evidenced by the disappearance of the 00ℓ basal peaks. Broad peaks, characteristic of nanocrystalline ZnO, were also observed. This is consistent with the formation of ZnO nanocrystals homogeneously dispersed in an amorphous aluminium-based oxide matrix.[37] The average crystallite size determined using the Rietveld[38] method was ≈6 nm.

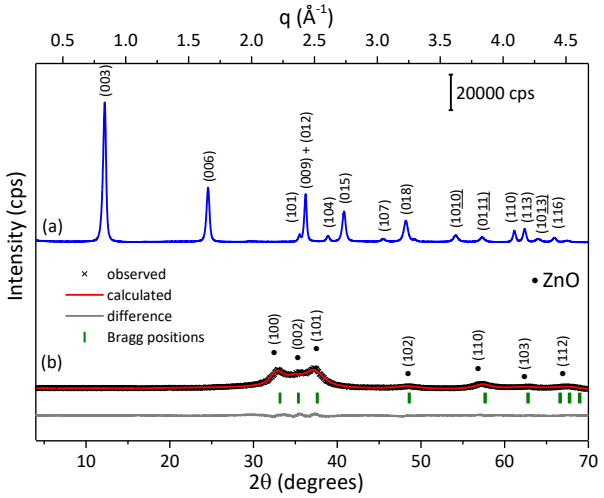

Fig. 2 XRD patterns of (a) LDH and (b) Calc-LDH.

N_2 adsorption/desorption isotherms of the sample before and after calcination are shown in Fig. 3. According to the IUPAC classification,[39] the absence of a plateau at the relative pressure region near to 1 is typical of type II isotherms and characteristic of macroporous material. In addition, the existence of a hysteresis between the adsorption and desorption isotherms shows the coexistence of mesopores.[39] The shape of the hysteresis loop concurs with the H3 type of IUPAC classification, which is usually associated with slit-shaped pores formed by platelet aggregation.

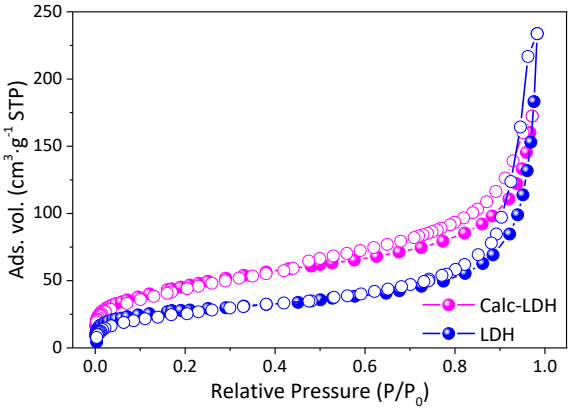

Fig. 3 N_2 adsorption (●)/desorption (○) isotherms of LDH and Calc-LDH.

In agreement with the slits-shape porosity, both materials present a wide pore size distribution with an average mesopore size (calculated by the ratio between the mesopore-specific volume and the specific surface area, *i.e.* $4V_p/S_{BET}$) of 17.7 nm and 5.4 nm, for LDH and Calc-LDH, respectively. It is noteworthy that after calcination a large increase was observed in the specific surface area from 74.4 m^2·g^{-1} (LDH) to 169.2 m^2·g^{-1} (Calc-LDH), because of the rearrangement of nanostructure induced by weight loss, reducing mesoporosity from 0.327 to 0.227 cm^3·g^{-1}. The obtained textural properties make these materials suitable for applications in adsorption process for species having molecular dimensions of 5 to 20 Å, such as the most common dye molecules.[40]

SEM and TEM images of pristine LDH are presented in Fig. 4a and 4b, respectively. For this material, it is possible to note the presence of hexagonal platelets forming aggregates with an open packing known as "sand rose", very common for LDH.[41] These platelets presented an average thickness around 37 nm. The SEM and TEM images of Calc-LDH are shown in Fig. 4c and 4d. For this material the platelets presented smaller sizes and thicknesses, forming shapeless aggregates with collapsed structure and becoming more densely packed.

3.2. Time-resolved monitoring of LDH thermal decomposition

The long-range order thermal evolution of LDH was monitored *in situ* by WAXS (Fig. 5). It is possible to note the progressive decrease in intensity of the (003) and (006) diffraction peaks with the increase in temperature. At temperatures between 220 and 300 °C we observed a displacement of the basal peak positions because of the loss of intercalated water, forming a dehydrated LDH phase. The LDH stacked structure was degraded completely at temperatures above 310 °C.

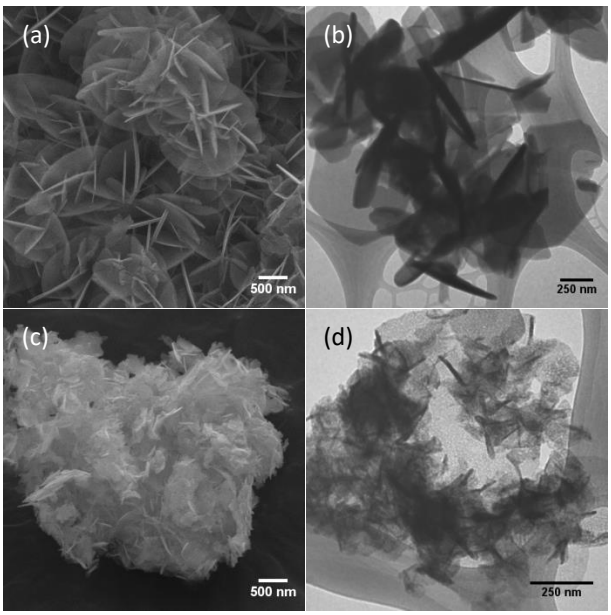

Fig. 4 Electron micrographs: (a) SEM and (b) TEM of pristine LDH, (c) SEM and (d) TEM of Calc-LDH.

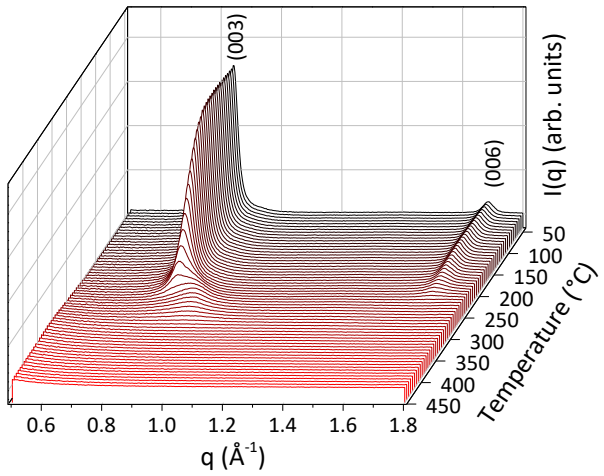

Fig. 5 WAXS patterns as a function of temperature during LDH thermal decomposition from RT to 450°C.

The change in the position of the WAXS diffraction peaks allowed us to calculate the variation of the interlayer distance as a function of temperature increase. The resulting evolution is compared with the thermogravimetric curves in Fig. 6. As discussed by Carvalho *et al.*,[42] LDH is thermally decomposed by four main steps: evaporation of weakly adsorbed water molecules from the crystallite surface, evaporation of the intercalated water between the layers, dehydroxylation coupled to transition metal oxide crystallization and anionic species decomposition. The first event occurs between RT and ≈150 °C, causing no significant changes in the basal spacing distance (d) found around 7.55 Å. The second occurs between 150 and ≈210 °C, with a small decrease of d from 7.55 to 7.48 Å due to the loss of intercalated water. The third event occurs from 210 to 310 °C and is related to the partial decomposition of the intercalated anion plus the dehydroxylation process, with a marked decrease in the basal spacing distance until the original lamellar structure is totally destroyed. Residual carbonate anion decomposition occurs at ≈520 °C.

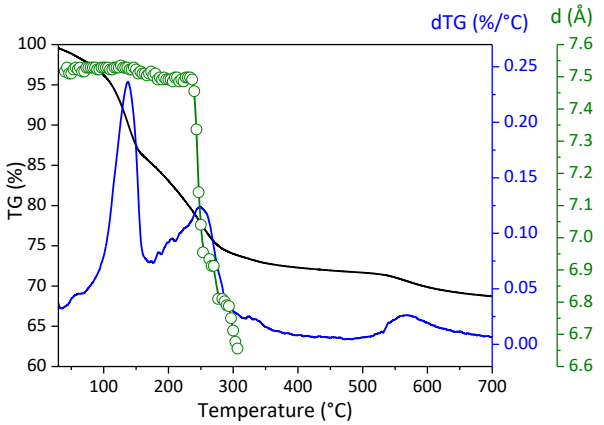

Fig. 6 Comparison of TG (black line) and dTG (blue line) curves with the interlamellar distance parameter (green symbol) obtained by WAXS.

The evolution of the LDH local range order during heating was investigated by Quick-XAS at the Zn K edge. Figs. 7a and 7b display the evolution of the XANES spectra recorded during heating from RT to 450°C and the non-phase corrected Fourier transforms (FT) of the EXAFS signals. Fig. 7a shows an invariance of the edge position, indicating that the Zn cations remain divalent during the thermal treatment, along with a change in the shape and intensity of the white line. Initially the FT presented two main contributions corresponding to the first octahedral oxygen coordination shell around Zn, at 2.05 Å (contribution at ≈1.65 Å on the FT) and the second nearest coordination shell, composed of Zn and Al atoms, at ≈3.10 Å (contribution at ≈2.75 Å on the FT) characteristic of the Zn arrangement in the pristine LDH. [42] Under heating, the FT evolved towards a mainly single shell oxygen contribution, initially located at the same distance as in the pristine LDH, and at shorter distance at higher temperature. The first evolution, which is dominant at the end of the dehydration step (≈220°C), corresponds to the formation of the dehydrated LDH structure as reported in [42]. The total breakdown of the lamellar structure leads to the formation of an amorphous mixed oxide phase at 450 °C, presenting a XANES fingerprint similar to that measured for the nanosized ZnO-like structure (Fig. S3). This interpretation is consistent with the shortening of the Zn-O distance observed when T > 300 °C, since for ZnO the Zn-O distance in the first coordination shell is equal to 1.96Å.[43]

The EXAFS signal and associated FT of the Calc-LDH sample measured at RT are presented in Fig. S4. Those signals are in phase with those of a crystalline ZnO reference compound displayed for comparison purposes. The presence of a second intense FT contribution for Calc-LDH when measured at RT (Fig. S4), compared to the intensity when measured at 450 °C

(Fig. 7b), results from the decrease of EXAFS signal damping associated to the decrease in thermal vibrations. The main parameters determined by EXAFS fitting of the two main contributions of the pristine LDH and Calc-LDH measured at RT are shown in Table S1. The formation of a nanosized ZnO-like phase was fully confirmed by least-square fitting, since the second neighbour contribution is composed of 12.1 ± 0.8 Zn atoms located at 3.24 Å. The coordination number found is in agreement with the crystallite size[43] of ≈6 nm determined by Rietveld refinement (see Fig. 2b). It is noteworthy that the Debye Waller factor of the Zn second nearest neighbour contribution for Calc-LDH is significantly higher (0.135 Å) than the one fitted for the bulk crystalline reference (0.097 Å). This suggests that a disordered ZnO network is formed upon LDH thermal decomposition.

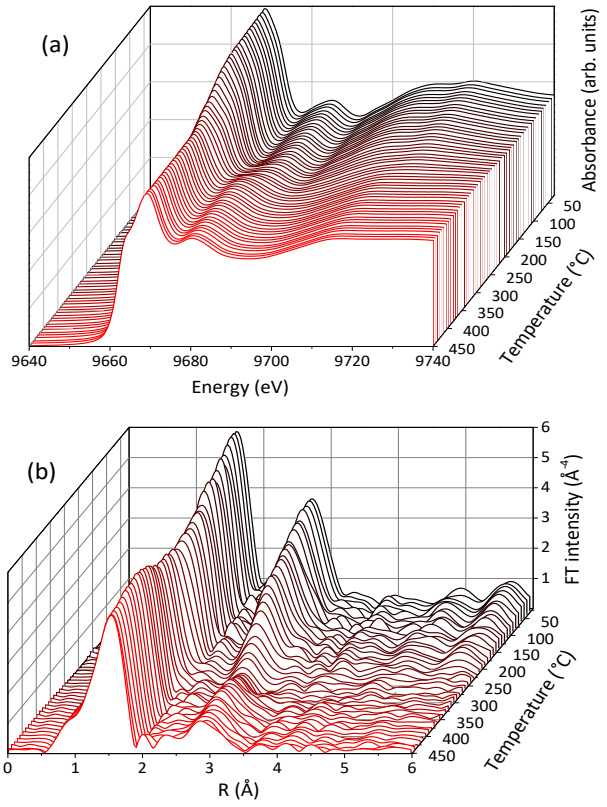

Fig. 7 Evolution of (a) Quick-XANES spectra at the Zn K edge measured *in situ* during LDH thermal decomposition and (b) corresponding FT of the EXAFS signals from RT to 450 °C.

The determination of the zinc species concentration profile was carried out using the MCR-ALS analysis assuming three pure components, as detailed in Supporting Information. The three components were identified as the pristine LDH, a dehydrated LDH phase and the nano-ZnO phase identified by the aforementioned fitting procedure. It is noteworthy that contrary to what was observed for the chlorine-LDH thermal decomposition,[42] the nano-$ZnAl_2O_4$ species was not identified for the present carbonate-intercalated material decomposed up to 450°C. The concentration profiles obtained for the pristine LDH, dehydrated LDH and nano-ZnO phases are shown (Fig. 8). The concentration of the dehydrated LDH phase increased from 100 to 225 °C and then declined until 350 °C due to the dehydroxylation process leading to the formation of nano-ZnO phase. In conclusion, these results indicate that nano-ZnO is the main Zn-based product of the thermal decomposition of the carbonate-LDH caused by heating to 450 °C.

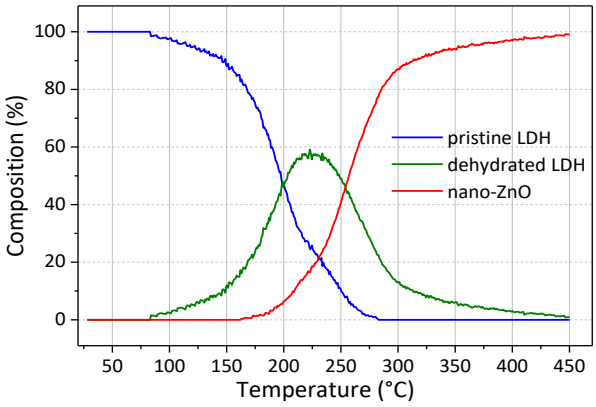

Fig. 8 Percentage of Zn based species determined from time-resolved Quick-XAS monitoring the LDH thermal decomposition.

3.3. Time-resolved monitoring of LDH recovery

The structural recovery of the LDH phase was investigated *in situ* by time-resolved WAXS and Quick-XAS measurements. Fig. 9 shows the time evolution of WAXS patterns monitored during the first hour of spontaneous recovery of the LDH lamellar structure induced by adding of water or aqueous dye solution to Calc-LDH. We observed the reappearance of the (003) and (006) diffraction signals after 2 min and 10 min contact with dye solution and water, respectively. The positions of those peaks are equal to the positions of the pristine LDH, where carbonate and hydroxyl anions are intercalated between LDH lamellae. Nevertheless, the intensity of the lines, normalized by an external standard, are less intense than those of the pristine LDH, suggesting either that the recovery is far from being complete or that the recovered LDH phase is less crystallized than the pristine LDH. Moreover, as the recovery time increased, the diffraction peaks became narrower, indicating crystallite growth perpendicular to the surface of layers. Assuming that peak broadening is due essentially to size effects, the width of the (003) Bragg peaks was used to calculate the average size of crystalline stacking from the classical Scherrer's equation:[44] $D = 0.89 \cdot \lambda / \beta \cdot \cos \theta$, where λ, θ and β are the X-ray wavelength (1.5406 Å), the Bragg diffraction angle and the line width at half maximum, respectively. The time evolution of the Quick-EXAFS data monitored during the spontaneous recovery of the LDH lamellar structure after the addition of water or dye aqueous solution to Calc-LDH is presented in Fig. S5. The change in FT contributions during LDH recovery is far from being as important as the modification observed during the thermal decomposition of pristine LDH (Fig. 6b). This is because the transformation is incomplete and the FT signals are a sum of nano-ZnO and recovered LDH with basically equivalent proportions after 3 h of recovery. The incomplete recovery of

ZnAl-LDH was also reported in literature,[45, 46] attributed to the higher crystallinity and the poorly reactivity of the formed ZnO in comparison to other oxides, usually MgO.[45] Moreover, after calcination, the local Al structure partially changes from octahedral to tetrahedral sites, which are not converted in LDH by rehydration.[46] The evolution of proportions of both phases as a function of time was determined by MCR-ALS analysis (Fig. S6).

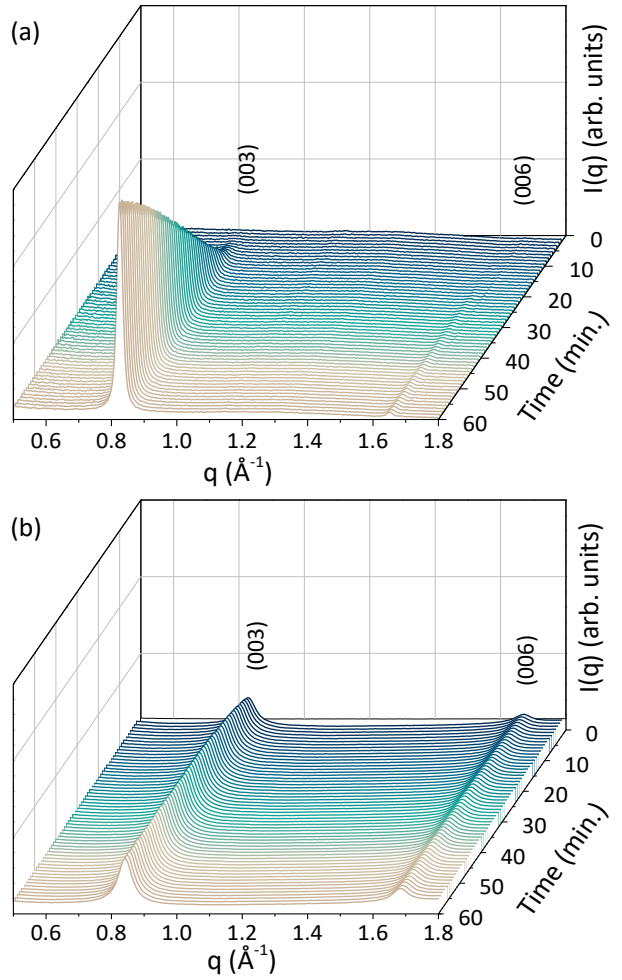

Fig. 9 WAXS *in situ* monitoring of the recovery at room temperature (≈25 °C) of the LDH phase after (a) water and (b) Acid Blue solution added to the Calc-LDH.

3.4. Mechanisms of LDH recovery

Fig. 10 compares the time evolution of the average crystalline size along the *c* direction, the integrated peak area, both determined from the (003) line and the amount of recovered LDH phase determined by MCR-ALS analysis of the Quick-XAS data. The XAS speciation evidences that the recovery induced by addition of water and dye solution shows comparable behaviour, with a huge increase in the proportion of LDH phase in the first hour, reaching about 30% and evolving asymptotically to a constant value (≈40%) after 120 min (Fig. S6). In the case of water addition, the recovery is made possible by rehydration process, since residual intercalated carbonate anions of the precursor LDH are still present in the Calc-LDH sample after calcination at 450°C and by hydroxyl anions from the water hydrolysis.[47] The similarities between both speciation curves indicate that the addition of the AB dye did not affect the kinetic of the LDH formation from the calcined sample. Indeed, the pseudo-first order kinetic model (continuous lines) described both experimental LDH speciation curves (k_1 = 5.1 x 10^{-4} s^{-1}). Thus the kinetics of LDH layer formation under water and AB dye addition are probably limited by the rate of dissolution/reprecipitation of the ZnO and Al_2O_3 nanoparticles. Since the solubility product, k_s, of $Al(OH)_3$, is almost 16 orders of magnitude lower than the ones of $Zn(OH)_2$ [at 25 °C, $k_s(Zn(OH)_2)$ = 4.1 x 10^{-17} and $k_s(Al(OH)_3)$ = 1.9 x 10^{-33}][48] the condensed Al^{3+} species are rapidly precipitated and the formation of LDH will be limited by the rate of Zn species precipitation, giving rise to the observed pseudo-first order reaction.

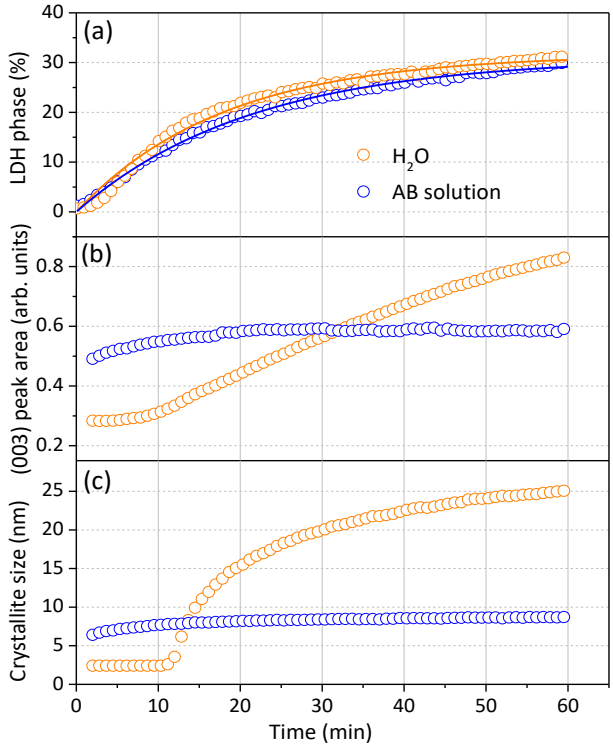

Fig. 10 Evolution as a function of the time of (a) the percentage of LDH phase, (b) the (003) peak area proportional to the stacked-LDH phase, and (c) the size of the crystalline stacking. Results reported in (a) are determined from XAS and those in (b) and (c) from WAXS, both measured during the first 60 min of LDH recovery by the addition of water (orange symbols) and dye solution (blue symbols) to Calc-LDH. Continuous lines in (a) are the fitting curves using a pseudo-first order kinetic model.

Unlike the XAS speciation, remarkable differences in the time evolution of the diffraction peak profile parameters characterising the crystalline stacking were observed for LDH recovery induced by contact with water or AB dye solution (Fig. 10b and 10c). On the one hand, after adding water, the amount (proportional to the peak area) and size of the crystallite present an initial induction period followed by a sigmoidal-like growth. According to the XAS speciation curve (Fig. 10a), the induction period occurs with a prompt formation of a significant amount of LDH species, which is classically associated to the nucleation step.[49, 50] On the other

hand, when the LDH is recovered by the AB dye solution addition, the nucleation step is too fast to be observed with the time resolution of the WAXS experiments (Fig. 10b). The advanced stages of LDH recovery with dye are characterised by a slight crystallite growth rapidly followed by a nearly unchanging peak area (Fig. 10b). and average crystallite size (Fig. 10c), characterising a steady-state regime. The observed sensitivity of nucleation and growth mechanisms with additives in aqueous solution is a strong indication of aggregative mechanisms.[49, 51] The behaviour observed herein is consistent with an aggregative nucleation and growth mechanism from exfoliated LDH lamellae or from small nanocrystals (tactoids) induced by the presence of the dye.

TEM images of Calc-LDH samples obtained after the first hour of regeneration in water and AB dye solution are presented in Fig. 11a and 11b, respectively. The image of sample regenerated in water shows well-formed hexagonal platelets, similar to those observed in pristine LDH (Fig 8b), evidencing the structural recovery of the LDH phase. The average thickness of platelets calculated by the fitting of experimental size distribution with a Gaussian function was 26 nm. This value is in good agreement with the average crystallite size along *c* direction (25 nm) determined from WAXS (Fig 10c). For the sample recovered in AB dye solution, the platelets presented smaller sizes and thicknesses compared to Calc-LDH regenerated in water. Again we found a reasonable agreement between the average platelet thickness (11 nm) determined from TEM images and average crystallite size (9 nm) determined from WAXS experiments after 60 min of recovery (Fig. 10c). These results confirm that the presence of AB dye in aqueous solution limits the stacking of the LDH layers, which is probably due to steric hindrance caused by the adsorption of the dye molecules. Despite several papers reporting different texture, morphology and crystallinity between pristine LDH and LDH recovered in presence of bulky dye anions,[21, 52, 53] the limitation of LDH growth caused by the adsorption of those molecules has not yet been reported.

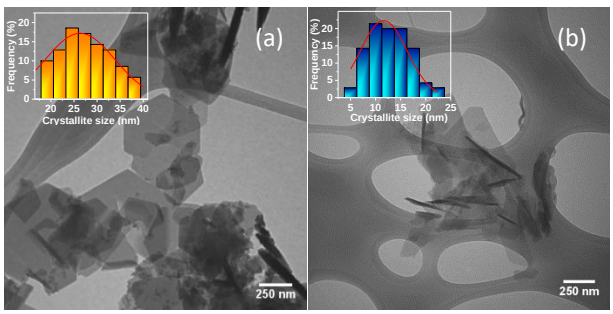

Fig. 11 TEM images and platelet thickness distributions (inserts) of Calc-LDH kept 60 min in contact with (a) water and (b) AB dye solution. The continuous lines in inserted graphs are the fitting curves assuming a Gaussian size distribution.

The different behaviours observed during LDH recovery with water or AB dye solution will be discussed on the basis of the regimes displayed in Fig. 12. Fig. 12a shows the dependency of the total amount of LDH phase, determined from XAS, with the cube of the crystallite size determined from the (003) WAXS lines assumed to be proportional to the crystallite volume. Fig. 12b displays the dependency of the cube crystallite size on the quantity of crystalline LDH, related to the integrated (003) peak area, hereafter referred to as stacked LDH. From those plots we intend to elucidate the LDH recovery mechanism and isolate the contribution related to the classical nucleation and growth mechanism from the aggregative process. In the classical mechanism, nuclei and nanocrystals of the thermodynamically stable phase (LDH) grow continuously only by the addition of atoms or molecules from the unstable phase (Calc-LDH) until reaching a steady-state chemical equilibrium. In an idealized aggregative process, nucleation and growth occur by accretion of pre-nuclei and coalescence of nanocrystals from the stable phase (LDH), respectively. Accordingly, the amount of LDH must remain constant during the increase of the cube of the average crystallite size along the (003) WAXS line.

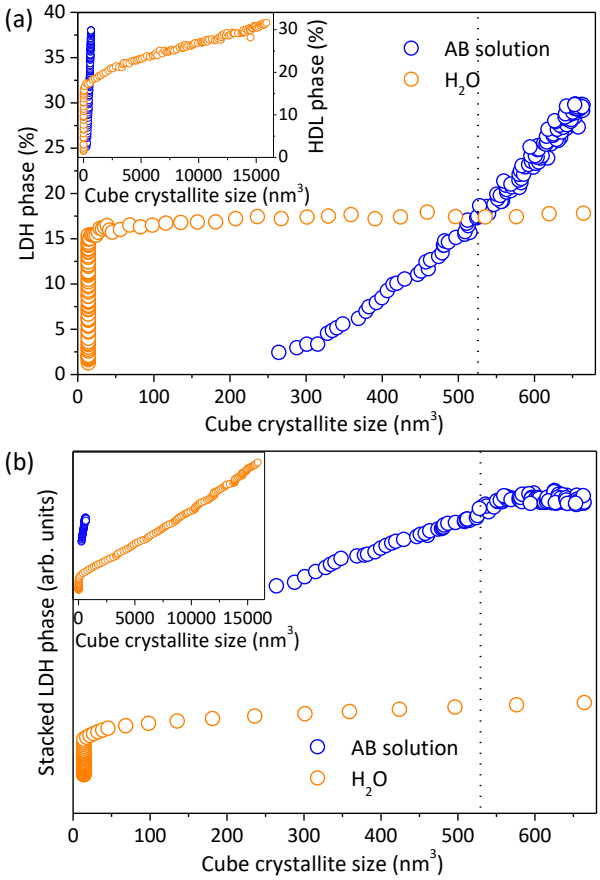

Fig. 12 Evolution of the LDH percentage determined by XAS (a) and the amount of stacked-LDH phase determined by WAXS (b) as a function of the cube particle size determined by WAXS, during the first 60 min of LDH recovery by the addition of water and dye solution to Calc-LDH.

The conditions expected for aggregative mechanism are in agreement with the two stages observed during the early period (t < 15min, Fig. 10) of recovery induced by ***water addition*** (see schematic diagram in Fig. 13a):

i) During the first step, the amount of LDH (total, Fig. 12a, and crystalline, Fig. 12b) increased, while the average size of the first detectable stacked LDH crystallites remained

essentially constant (≈2.5 nm) until 10 min of reaction. This indicates that the number of LDH nanocrystals increases, confirming the nucleation process. The time invariance of the nanocrystal size is a strong evidence of aggregative nucleation involving the oriented attachment along the *c*-axis of newly formed LDH lamellae pre-nuclei.

ii) In the second step the crystallite size increased without a great change in the amount of LDH, evidencing coalescence by the oriented stacking of LDH nanocrystals.

The insert in Fig. 12, which expands the data over the full time period presented in Fig. 10, highlights the strong deviation from pure coalescence mechanism revealed by the nearly linear increase of the total amount of LDH and of crystalline stacked LDH observed for t > 15 min (Fig. 10). This finding evidences a continuous accretion of newly formed LDH lamellae to the growing stacked nanocrystal. To the best of our knowledge, there are no works in literature reporting the LDH recovery mechanism by aggregative models. In fact these non-classical nucleation and growth mechanisms are sometimes invoked to explain the advanced step of hydrothermal LDH synthesis.[48]

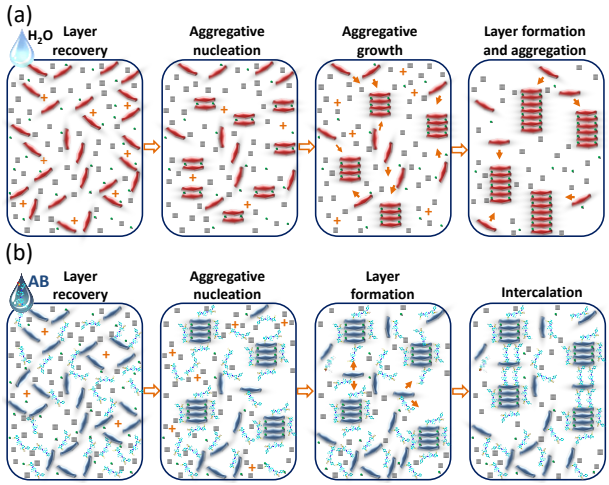

Fig. 13 Scheme of the LDH recovery induced by (a) water and (b) AB dye solution addition.

When the LDH is recovered by ***AB dye solution addition*** (Fig. 13b) only the advanced stage is observed, characterised by the continuous accretion of the newly formed LDH lamellae on the growing stacked nanocrystal. Moreover, the latter advanced stage is characterised by the invariance of the amount of crystalline stacked LDH phase and the associated increase of the percentage of total LDH species. This finding indicates that the newly formed LDH lamellae are not stacked in a periodic array. The coexistence of nanocrystalline LDH with an increased amount of exfoliated LDH layer suggests that the AB dye adsorption hinders the aggregative growth of the stacked LDH nanocrystal.

The long-term structural evolution during recovery in the presence of the AB dye solution was analysed from *ex-situ* XRD results (Fig. 14a) in order to evaluate the possible intercalation of AB anions into the interlayer galleries. As shown, the XRD patterns of Calc-LDH at different times of dye adsorption evidenced the reappearance of the peaks □(003) and □(006) whose positions correspond with the basal spacing distance of 7.52 Å characteristic of the intercalation of carbonate and hydroxyl anions on the interlayer domain. At ≈180 min of contact time, it is possible to note an ill-defined low angle diffraction peak, Δ(003), attributed to the Acid Blue intercalation on the LDH. The basal spacing distance of 22.3 Å corresponding to this peak suggests an intercalation of AB dye with a configuration similar to that proposed in Fig. 14b.[13]

The aforementioned recovery behaviour supports the hypothesis of the LDH-recovery mechanism by direct synthesis as early proposed by Mascolo and Mascolo,[16] since the presence of the anionic species changes the kinetics of the aggregative nucleation and growth processes. We observed that the presence of bulky organic anion (AB) assisted the formation of the LDH pre-nuclei lamellae and growth through oriented attachment of lamellae incorporating carbonate anions in the interlamellar space, but also strongly limited growth along c-axis by the steric hindrance caused by the adsorption of bulky organic molecules on the external crystallite surface. This size-limitation phenomenon of the recovered-LDH particles explains the higher adsorption capacity of organic anionic species using calcined LDH compared to pristine-LDH, since the recovered structure had a greater contact area for adsorption on the external surface. Additionally, the adsorption of dye in the internal structure of the aggregates and between the interlamellar spaces can contribute to the high adsorption capacity of Calc-LDH. In the next section we compare the adsorption capacity of the calcined and pristine material.

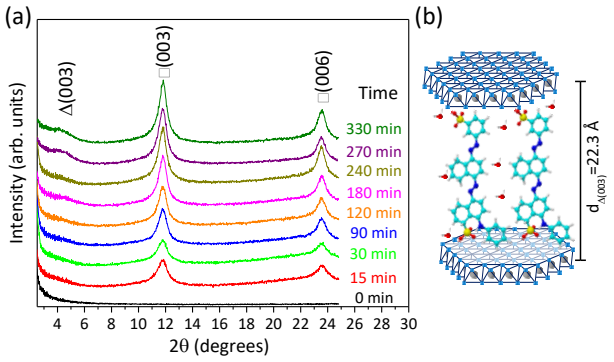

Fig. 14 (a) XRD patterns of Calc-LDH during different contact times with AB dye solution and (b) possible configuration of AB anions intercalated on recovered LDH structure.

3.5. Dye adsorption on LDH and Calc-LDH

Evolution of the amount of dye, adsorbed by pristine-LDH and Calc-LDH, as a function of time is shown in Fig. 15. The adsorption capacity of Calc-LDH is six times higher than the pristine material, which can be explained by the lower crystallite size of recovered material (Fig. 4b and 11b). In fact we can expect an increase of external surface area of five times, caused by the four times reduction of the average

crystallite size (9 nm) of LDH recovered in dye solution as compared to the pristine one (37 nm).

A two-stepped kinetic was observed for the Calc-LDH compared to the single kinetic for pristine-LDH. The amount of dye adsorbed by both pristine and Calc-LDH rapidly increases during the first hour and reaches a first equilibrium state around 2 h. In the Calc-LDH, this first step is immediately followed by a second increase of adsorbed dye, reaching a plateau after 8 h. The first step is related to the adsorption on the external surface of the recovered material. The second adsorption step is attributed to the adsorption of the azo dye anions onto the inner surface of the aggregates but also to the intercalation between recovered LDH lamellae as evidenced by XRD (Fig. 14). Both inner dye accumulation processes characterising the second step are limited by the intra-particle diffusion mechanism.[54]

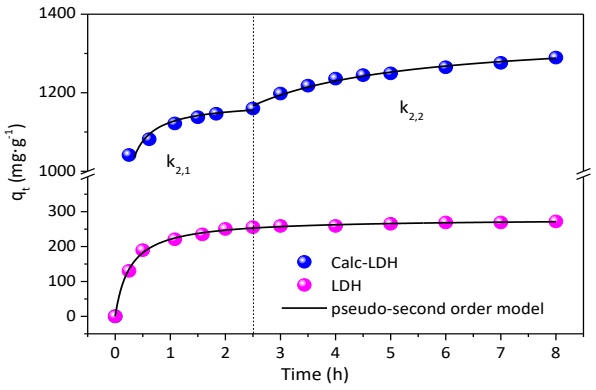

Fig. 15 Effect of contact time on adsorption using a 1000 mg·L^{-1} initial dye concentration on LDH and Calc-LDH (T = 25 °C, dosage = 500 mg·L^{-1}).

The azo dye anions adsorption on external (step 1) and internal (step 2) surfaces have been described by pseudo-second order kinetics with constant rates $k_{2,1}$ and $k_{2,2}$ (Table S2). Regardless of the adsorbent material, the kinetic constant $k_{2,1}$ is of the same order of magnitude (≈1.5 10^{-2} g mg^{-1} h^{-1}), evidencing that this kinetic step is governed by the same adsorption process, *i.e.*, on the external surface of already-built LDH aggregates (pristine LDH) or of on-going rebuilding LDH aggregates (Calc-LDH). The dye adsorption capacity at the steady-state first equilibrium q_{e1} is about four time higher for Calc-LDH, which is mainly caused by the instantaneous differences between the specific surfaces of rebuilding (Calc-LDH) and pristine LDH. It is noteworthy that the $k_{2,2}$ constant rate (1.9 10^{-3} g mg^{-1} h^{-1}) for Calc-LDH is one order of magnitude lower than the $k_{2,1}$ rate. This finding is fully consistent with our interpretation of adsorption being limited by the intra-particles diffusion. The ratio between q_{e1} and q_{e2} indicates that the contribution of adsorption on the internal surface (including interaction) is about 13% for Calc-LDH and insignificant for pristine LDH.

Fig. 16 compares the dye adsorption isotherms for LDH and Calc-LDH materials. The adsorption capacity of both materials increases with the increase in initial dye concentration in the aqueous phase, gradually reaching saturation at high concentrations. A higher adsorption capacity is observed for the Calc-LDH compared to the pristine LDH. The same observations were reported in the literature for MgAl-LDH.[13, 19, 40] The lines reported in Fig. 16 correspond to the fit of experimental data using either the Langmuir or the Freundlich model. The best fit was obtained with the Langmuir isotherm equation indicating that the adsorption process is limited to a dye monolayer and that at the steady state equilibrium all surface adsorption sites have comparable adsorption heat. Taking into account the phase heterogeneity after calcination (nano-ZnO and amorphous Al_2O_3) and the steady state of the recovery (60% of (nano-ZnO and amorphous Al_2O_3) and 40% of recovered LDH), the good fit with the Langmuir model provides strong evidence that the surface adsorption sites studied belong mainly to the recovered LDH.

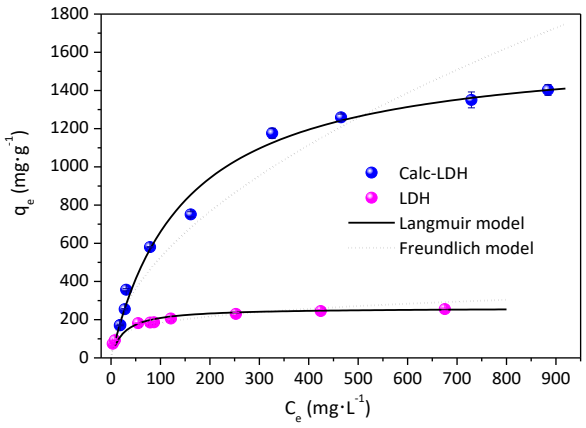

Fig. 16 Adsorptions isotherms at 25 °C using LDH and Calc-LDH (pH = 7.0; adsorbent dosage = 500 mg·L^{-1}) and fits either the Langmuir or Freundlich model.

The Langmuir parameters determined from the fit of the experimental dye adsorption isotherms for LDH and Calc-LDH materials are shown in Table S3. The monolayer adsorption capacity for Calc-LDH was approximately 6 times higher than that of the pristine LDH material: 1587 mg·g^{-1} (2.33 mmol·g^{-1}) and 261.8 mg·g^{-1} (0.384 mmol·g^{-1}) at 25 °C. The k_L parameter value obtained for LDH was higher than that obtained for Calc-LDH, corresponding to the lower energy requirement for the process using the calcined material and providing greater removal rates under normal RT conditions.

The effect of temperature on the isotherm adsorption of the dye was evaluated using the Langmuir model for pristine LDH and Calc-LDH. Using the fitted k_L values (Table S2), the Langmuir equilibrium constant k_{ad} was determined and used to build the Van't Hoff plot. The enthalpy and entropy of the process were derived from the slope and instantaneous intercept of the linear dependence described by the Van't Hoff equation (Fig. S7). The obtained values are shown in Table 1.

The positive value for the enthalpy change (ΔH°) is related to the endothermic nature of the process and the positive value of the change in entropy (ΔS°) suggests an increase of the disorder at the solid-solution interface. Negative values obtained for the change in Gibbs free energy (ΔG°) show that the adsorbed forms are more stable than those in solution. Thus, the adsorption process occurs spontaneously.[35] It is interesting to note that the enthalpy and entropy values for

the Calc-LDH are about 60% lower than the pristine-LDH values. This finding is consistent with the proportion of recovered LDH at the equilibrium determined around 40% by EXAFS (Fig. S5). This is an additional independent evidence that the dye adsorption essentially occurs on the surface of recovered LDH particles.

Finally, it is important to highlight that the initial properties of Calc-LDH sample used in the adsorption experiments were recovered after thermal treatment at 450 °C for 30 min under air flow. Under these conditions the adsorbed AB dye can be decomposed, and the adsorbent is recycled. The AB adsorption on Calc-LDH was tested in five regeneration cycles (Fig. S8). After the first use, the adsorption capacity reached 93, 92, 91, and 91 % of the initial capacity. This small reduction in adsorption capacity, indicates an important reuse property of the LDH memory effect. Other studies have also shown good recyclabilities for different LDH compounds and diverse anionic dye molecules.[9, 52]

Table 1 Thermodynamic properties calculated for the adsorption process at 25°C.

Material	ΔG° ($kJ \cdot mol^{-1}$)	ΔH° ($kJ \cdot mol^{-1}$)	ΔS° ($kJ \cdot K^{-1} \cdot mol^{-1}$)
LDH	-26.4	44.4	0.239
Calc-LDH	-21.5	25.5	0.158

4. Conclusions

The paper revisits the use of LDH and of its thermal decomposition product as efficient adsorbent for environmental application, using as model system the removal of Acid Blue 113 (AB) dye from aqueous solutions. The calcined LDH showed an adsorption capacity approximately six times greater than the pristine LDH, highlighting the synergic cooperation of dye adsorption and the so-called "LDH memory effect".

The comparison between the recovery in water and in AB dye solution evidences that the LDH recovery followed the same pseudo-first order kinetic limited by the dissolution and re-precipitation of ZnO species. The recovery of the LDH nanostructure is driven by an aggregative nucleation and growth mechanism. The steric hindrance caused by adsorbed dye limits the stacking of the lamellae, leading to a mixture of small crystalline tactoids and aggregates of exfoliated LDH.

The kinetic of dye adsorption on Calc-LDH shows two-step behaviour consistent with the dye adsorption on the external and internal surfaces of ongoing recovered LDH lamellar aggregates. The intercalation of anionic dye in the interlayer LDH galleries is only verified after ≈180 min of contact with the dye solution, contributing merely with 13% of the adsorption capacity. The adsorption isotherms follow the Langmuir model, confirming that the adsorption takes place mainly on the reconstructed LDH external surface. LDH memory effect allows the efficient recyclability of the used LDH adsorbent.

Acknowledgements

The authors are grateful for the financial support received from the Brazilian agencies CAPES, CNPq, and FAPESP (Processes 2013/25043-4 and 2015/23410-5). We also thank the Brazilian Synchrotron Light Laboratory (LNLS) for the WAXS experiments provided at the SAXS1 beamline and the Synchrotron SOLEIL (France) to the Quick-XAS experiments at the ROCK beamline, which was supported by a public grant overseen by the French National Research Agency (ANR) as part of the *"Investissements d'Avenir"* Program (reference: ANR-10-EQPX-45). This work is also a collaborative research project of the members of the Rede Mineira de Química (RQ-MG) supported by FAPEMIG (Project: CEX - RED-00010-14).

References

1. D. T. Sponza and M. Işık, *Enzyme and Microbial Technology*, 2004, **34**, 147-158.
2. A. Ahmad, S. H. Mohd-Setapar, C. S. Chuong, A. Khatoon, W. A. Wani, R. Kumar and M. Rafatullah, *RSC Advances*, 2015, **5**, 30801-30818.
3. C. O'Neill, F. R. Hawkes, D. L. Hawkes, S. Esteves and S. J. Wilcox, *Water Research*, 2000, **34**, 2355-2361.
4. J. L. Figueiredo, J. P. S. Sousa, C. A. Orge, M. F. R. Pereira and J. J. M. Órfão, *Adsorption*, 2010, **17**, 431-441.
5. E. M. Seftel, M. Niarchos, C. Mitropoulos, M. Mertens, E. F. Vansant and P. Cool, *Catalysis Today*, 2015, **252**, 120-127.
6. J.-W. Lee, S.-P. Choi, R. Thiruvenkatachari, W.-G. Shim and H. Moon, *Water Research*, 2006, **40**, 435-444.
7. H. Selcuk, *Dyes and Pigments*, 2005, **64**, 217-222.
8. N. A. Khan, Z. Hasan and S. H. Jhung, *Journal of Hazardous Materials*, 2013, **244–245**, 444-456.
9. M. A. Ulibarri, I. Pavlovic, C. Barriga, M. C. Hermosín and J. Cornejo, *Applied Clay Science*, 2001, **18**, 17-27.
10. G. Fan, F. Li, D. G. Evans and X. Duan, *Chemical Society Reviews*, 2014, **43**, 7040-7066.
11. G. R. Williams and D. O'Hare, *Journal of Materials Chemistry*, 2006, **16**, 3065-3074.
12. A. I. Khan, L. Lei, A. J. Norquist and D. O'Hare, *Chemical Communications*, 2001, 2342-2343.
13. G. Bascialla and A. E. Regazzoni, *Colloids and Surfaces A: Physicochemical and Engineering Aspects*, 2008, **328**, 34-39.
14. M.-X. Zhu, Y.-P. Li, M. Xie and H.-Z. Xin, *Journal of Hazardous Materials*, 2005, **120**, 163-171.
15. E. L. Crepaldi, J. Tronto, L. P. Cardoso and J. B. Valim, *Colloids and Surfaces A: Physicochemical and Engineering Aspects*, 2002, **211**, 103-114.
16. G. Mascolo and M. C. Mascolo, *Microporous and Mesoporous Materials*, 2015, **214**, 246-248.
17. F. Millange, R. I. Walton and D. O'Hare, *Journal of Materials Chemistry*, 2000, **10**, 1713-1720.
18. T. Sato, H. Fujita, T. Endo, M. Shimada and A. Tsunashima, *Reactivity of Solids*, 1988, **5**, 219-228.

19. R. M. M. Santos, R. G. L. Goncalves, V. R. L. Constantino, L. M. Costa, L. H. M. Silva, J. Tronto and F. G. Pinto, *Applied Clay Science*, 2013, **80-81**, 189-195.
20. Z. Li, B. Yang, S. Zhang, B. Wang and B. Xue, *Journal of Materials Chemistry A*, 2014, **2**, 10202-10210.
21. Y. Guo, Z. Zhu, Y. Qiu and J. Zhao, *Chemical Engineering Journal*, 2013, **219**, 69-77.
22. F. Cavani, F. Trifirò and A. Vaccari, *Catalysis Today*, 1991, **11**, 173-301.
23. E. P. Barrett, L. G. Joyner and P. P. Halenda, *Journal of the American Chemical Society*, 1951, **73**, 373-380.
24. C. A. Schneider, W. S. Rasband and K. W. Eliceiri, *Nat Meth*, 2012, **9**, 671-675.
25. V. Briois, C. La Fontaine, S. Belin, L. Barthe, T. Moreno, V. Pinty, A. Carcy, R. Girardot and E. Fonda, *Journal of Physics: Conference Series*, **712**, 1-6.
26. E. Fonda, A. Rochet, M. Ribbens, L. Barthe, S. Belin and V. Briois, *Journal of Synchrotron Radiation*, 2012, **19**, 417-424.
27. C. La Fontaine, L. Barthe, A. Rochet and V. Briois, *Catalysis Today*, 2013, **205**, 148-158.
28. J. Jaumot, R. Gargallo, A. de Juan and R. Tauler, *Chemometrics and Intelligent Laboratory Systems*, 2005, **76**, 101-110.
29. W. H. Cassinelli, L. Martins, A. R. Passos, S. H. Pulcinelli, C. V. Santilli, A. Rochet and V. Briois, *Catalysis Today*, 2014, **229**, 114-122.
30. J. Hong, E. Marceau, A. Y. Khodakov, L. Gaberová, A. Griboval-Constant, J.-S. Girardon, C. L. Fontaine and V. Briois, *ACS Catalysis*, 2015, **5**, 1273-1282.
31. A. Rochet, B. Baubet, V. Moizan, C. Pichon and V. Briois, *Comptes Rendus Chimie*, 2016, **19**, 1337-1351.
32. M. Staniuk, O. Hirsch, N. Kränzlin, R. Böhlen, W. van Beek, P. M. Abdala and D. Koziej, *Chemistry of Materials*, 2014, **26**, 2086-2094.
33. B. Ravel and M. Newville, *Journal of Synchrotron Radiation*, 2005, **12**, 537-541.
34. W. Plazinski, W. Rudzinski and A. Plazinska, *Advances in Colloid and Interface Science*, 2009, **152**, 2-13.
35. Q. Yu, Y. Zheng, Y. Wang, L. Shen, H. Wang, Y. Zheng, N. He and Q. Li, *Chemical Engineering Journal*, 2015, **260**, 809-817.
36. S. Miyata, *Clays & Clay Minerals*, 1983, **31**, 305-311.
37. X. Zhao, L. Wang, X. Xu, X. Lei, S. Xu and F. Zhang, *AIChE Journal*, 2012, **58**, 573-582.
38. H. Rietveld, *Journal of Applied Crystallography*, 1969, **2**, 65-71.
39. C. V. Santilli and S. H. Pulcinelli, *Cerâmica*, 1993, **39**, 11-16.
40. A. R. Auxilio, P. C. Andrews, P. C. Junk and L. Spiccia, *Dyes and Pigments*, 2009, **81**, 103-112.
41. Q. Wang, Y. Gao, J. Luo, Z. Zhong, A. Borgna, Z. Guo and D. O'Hare, *RSC Advances*, 2013, **3**, 3414-3420.
42. H. W. P. Carvalho, S. H. Pulcinelli, C. V. Santilli, F. Leroux, F. Meneau and V. Briois, *Chemistry of Materials*, 2013, **25**, 2855-2867.
43. M. S. Tokumoto, S. H. Pulcinelli, C. V. Santilli and V. Briois, *The Journal of Physical Chemistry B*, 2003, **107**, 568-574.
44. A. L. Patterson, *Physical Review*, 1939, **56**, 978-982.
45. Y. Lin, Q. Fang and B. Chen, *Journal of Environmental Sciences*, 2014, **26**, 493-501.
46. A. Vyalikh, F. R. Costa, U. Wagenknecht, G. Heinrich, D. Massiot and U. Scheler, *The Journal of Physical Chemistry C*, 2009, **113**, 21308-21313.
47. O. D. Pavel, R. Zăvoianu, R. Bîrjega, E. Angelescu, G. Costentin and M. Che, *Applied Clay Science*, 2015, **104**, 59-65.
48. X. Sun and S. K. Dey, *Journal of Colloid and Interface Science*, 2015, **458**, 160-168.
49. F. Wang, V. N. Richards, S. P. Shields and W. E. Buhro, *Chemistry of Materials*, 2014, **26**, 5-21.
50. J. J. De Yoreo and P. G. Vekilov, *Reviews in Mineralogy and Geochemistry*, 2003, **54**, 57.
51. J. F. Banfield, S. A. Welch, H. Zhang, T. T. Ebert and R. L. Penn, *Science*, 2000, **289**, 751.
52. R. M. M. d. Santos, R. G. L. Gonçalves, V. R. L. Constantino, C. V. Santilli, P. D. Borges, J. Tronto and F. G. Pinto, *Applied Clay Science*, 2017, **140**, 132-139.
53. R. Extremera, I. Pavlovic, M. R. Pérez and C. Barriga, *Chemical Engineering Journal*, 2012, **213**, 392-400.
54. Y. X. Zhang, X. D. Hao, T. Wang, Y. X. Meng and X. Han, *Dalton Transactions*, 2014, **43**, 6667-6676.

